

Noble Metal-Like Behavior of Plasmonic Bi Particles as a Cocatalyst Deposited on $(\text{BiO})_2\text{CO}_3$ Microspheres for Efficient Visible Light Photocatalysis

Fan Dong,*[†] Qiuyan Li,[†] Yanjuan Sun,[†] and Wing-Kei Ho*^{,‡}

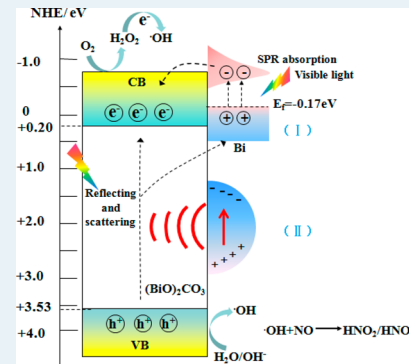
[†]Chongqing Key Laboratory of Catalysis and Functional Organic Molecules, College of Environmental and Biological Engineering, Chongqing Technology and Business University, 400067 Chongqing, People's Republic of China

[‡]Department of Science and Environmental Studies, The Centre for Education in Environmental Sustainability, The Hong Kong Institute of Education, 10 Lo Ping Road, Tai Po, New Territories, Hong Kong, People's Republic of China

S Supporting Information

ABSTRACT: Novel plasmonic Bi nanoparticles deposited *in situ* in $(\text{BiO})_2\text{CO}_3$ microspheres (Bi/BOC) were fabricated via a one-pot hydrothermal treatment of bismuth citrate, sodium carbonate, and thiourea. Different characterization techniques, including XRD, SEM, TEM, XPS, UV-vis DRS, PL, time-resolved fluorescence spectra, and photocurrent generation, were performed to investigate the structural and optical properties of the as-prepared samples. The results indicated that the Bi nanoparticles were generated on the surface of $(\text{BiO})_2\text{CO}_3$ microspheres via the *in situ* reduction of Bi^{3+} by thiourea. The Bi nanoparticle deposited $(\text{BiO})_2\text{CO}_3$ microspheres were employed for the photocatalytic removal of NO in air under visible light irradiation, and the sample exhibited a drastically enhanced photocatalytic activity and oxidation ability. The highly enhanced activity was attributed to the cooperative contribution of the surface plasmon resonance (SPR) effect, the efficient separation of electron–hole pairs, and the prolonged lifetime of charge carriers by the Bi nanoparticles. The behavior of Bi nanoparticles as a cocatalyst for enhancing photocatalytic activity is similar to that of noble metals in photocatalysis. When the amount of thiourea was controlled at 5%, the corresponding Bi/BOC sample exhibited the highest photocatalytic activity and exceeded those of other types of visible light photocatalysts, such as nonmetal-doped TiO_2 , C_3N_4 , BiOBr , N-doped $(\text{BiO})_2\text{CO}_3$, and even Ag-deposited $(\text{BiO})_2\text{CO}_3$. The visible light photocatalytic activity of Bi/BOC was also tested at different wavelengths and with different light sources. It was found that the high activity could be well maintained even under a 5 W energy-saving light, demonstrating its great potential in practical applications. On the basis of DMPO-ESR spin trapping, the active species produced from Bi/BOC under visible light were hydroxyl radicals. Bi/BOC could produce more hydroxyl radicals in comparison to BOC due to the SPR effect of Bi, contributing to the enhanced oxidation ability. Furthermore, the Bi/BOC sample displayed a high photochemical stability under repeated irradiation. This work demonstrated the great feasibility of utilizing low-cost Bi nanoparticles as a substitute for noble metals to enhance visible light photocatalysis.

KEYWORDS: plasmonic Bi nanoparticles, $(\text{BiO})_2\text{CO}_3$ microspheres, hydrothermal method, SPR effect, visible light photocatalysis, charge separation



1. INTRODUCTION

Photocatalysis technology has attracted enormous interest because it is an economical and environmentally friendly technology that can be applied in environmental remediation, solar energy conversion, and organic photosynthesis.^{1–5} Various types of semiconductor photocatalysts have been developed.^{6–8} Specifically, TiO_2 -based photocatalysts have been widely investigated.^{9,10} However, the rapid recombination rate of electron–hole pairs and the low utilization of solar energy on TiO_2 photocatalysts result in low photocatalytic activity.¹¹ Therefore, the development of photocatalysts with outstanding visible light activity is urgent and indispensable.

Bismuth is a semimetal that has a very small band overlap and possesses interesting surface plasmon resonance (SPR)

properties.¹² Various nanostructured Bi species have been synthesized for nanocatalysis and optical applications.^{13–17} Recently, Bi was also found to show photocatalytic activity.^{18–22} We have discovered the direct plasmonic photocatalysis of Bi element mediated by SPR for NO removal.²² Given the high cost of noble metals, inexpensive Bi with its unique properties can be an alternative (SPR effect and electron trap) in the photocatalytic process. The synthesis and modification of Bi-based semiconductor photocatalysts has attracted intense research interest.^{23–25} Several Bi element

Received: July 20, 2014

Revised: October 27, 2014

Published: October 30, 2014

deposited photocatalysts have been reported, such as Bi/Bi₂O₃,²⁶ Bi/BiOCl,^{27,28} and Bi/BiOI.²⁹ These nanocomposite photocatalysts exhibit enhanced photocatalytic activity in comparison with their separate components due to the existence of Bi.

As a bismuth-containing semiconductor photocatalyst, (BiO)₂CO₃ has received great research interest because of its attractive morphology and high photocatalytic activity. Chen and co-workers prepared (BiO)₂CO₃ nanotubes, nanobars, nanoplates, and nanocubes via a simple reflux or solvothermal/hydrothermal process.^{30,31} Xie's group also synthesized various (BiO)₂CO₃ microstructures for the degradation of the aqueous dye Rhodamine B (RhB).³² (BiO)₂CO₃ nanosheets and flowerlike structures were prepared by Huang et al.³³ Cao's group fabricated persimmon-like (BiO)₂CO₃, which displayed efficient photocatalytic activity for the degradation of RhB and eosin sodium salt under simulated solar light irradiation.³⁴ Yu and co-workers reported on BiVO₄/(BiO)₂CO₃ and graphene/(BiO)₂CO₃ nanocomposites with enhanced visible light photocatalytic activity.^{35,36} Our research team fabricated N-doped (BiO)₂CO₃ and Ag-deposited (BiO)₂CO₃ hierarchical microspheres, which exhibited outstanding photocatalytic activity for the degradation of NO in air under visible light irradiation.^{37–40} Given the noble-metal-like behavior of Bi, developing Bi/(BiO)₂CO₃ nanocomposites to enhance photocatalysis efficiency has drawn significant interest. To date, studies on Bi nanoparticle-deposited (BiO)₂CO₃ microspheres have never been reported.

In this study, we developed a one-pot hydrothermal method to deposit Bi in situ as cocatalyst on (BiO)₂CO₃ microspheres. During the hydrothermal reaction, thiourea functioned as a reductant and easily reduced Bi³⁺ to metallic Bi. Photocatalytic activity tests for NO removal were carried out to investigate the activity variation of the sample after metallic Bi deposition. The results showed a drastically enhanced visible light photocatalytic activity which was much higher than that of pure (BiO)₂CO₃ and Bi because of the SPR effect, efficient separation of electron–hole pairs, and prolonged lifetime of charge carriers by Bi nanoparticles. The catalytic behavior of Bi nanoparticles as a cocatalyst is similar to that of noble metals. Meanwhile, the as-prepared samples exhibited decent photochemical stability and could work under low-energy lamps, which are significant for their practical applications. The present work demonstrated the possibility for the utilization of low-cost Bi nanoparticles as a substitute for noble metals to improve the performance of other photocatalytic materials.

2. EXPERIMENTAL SECTION

2.1. Synthesis. All of the reagents employed in this study were of analytical grade and were used without further purification. In a typical synthesis process, sodium carbonate (0.46 g) was first dissolved in distilled water (70 mL) in a 100 mL autoclaved Teflon vessel and the mixture was then stirred for 10 min. An appropriate volume of 0.04 mol/L thiourea solution was then added, and the resulting solution was stirred further for 10 min. The amounts of thiourea solution added were 0.5, 2.5, and 5.0 mL. Afterward, bismuth citrate (1.6 g) was added to the solution, and the mixture was stirred for 30 min to ensure that all reagents were dissolved. The resulting precursor suspension was hydrothermally treated at 160 °C for 24 h. After the mixture was cooled to room temperature, the resulting solid was filtered, washed with water and ethanol four times, and dried at 60 °C for 12 h to obtain the final sample.

The mass ratios of thiourea to (BiO)₂CO₃ were controlled at 1%, 5%, and 10%, and the resulting samples were labeled as Bi/BOC-1, Bi/BOC-5, and Bi/BOC-10, respectively. Pure (BiO)₂CO₃ microspheres and Bi nanoparticles were also prepared as references and labeled as BOC and Bi, respectively.^{22,39}

2.2. Characterization. The X-ray diffraction (XRD) patterns of the samples were obtained using an X-ray diffractometer equipped with intense Cu K α radiation (Model D/max RA, Rigaku Co., Japan). The morphology, structure, and chemical composition of the obtained products were analyzed using a scanning electron microscope (SEM-EDX, JEOL Model JSM-6490, Japan), a transmission electron microscope (TEM, JEM-2010, Japan), and a high-resolution transmission electron microscope (HRTEM). The Brunauer–Emmett–Teller (BET) specific surface areas (S_{BET}) of the samples were determined using a nitrogen adsorption apparatus (ASAP 2020, USA) with all samples degassed at 100 °C for 12 h prior to measurements. X-ray photoelectron spectroscopy (XPS) measurements were carried out to investigate the surface chemical compositions and states with Al K α X-ray ($h\nu = 1486.6$ eV) radiation source operated at 150 W (Thermo ESCALAB 250, USA). The UV–vis diffuse reflection spectra (UV–vis DRS) were obtained for the dry-pressed disk samples by using a Scan UV–vis spectrophotometer (UV-2450, Shimadzu, Japan) with 100% BaSO₄ as the standard sample. Photoluminescence (PL, F-7000, Hitachi, Japan) was used to investigate the optical properties of the obtained samples. The steady and time-resolved fluorescence emission spectra were recorded at room temperature by using a fluorescence spectrophotometer (Edinburgh Instruments, FLSP-920). The sample for ESR measurement (FLSp920, England) was prepared by mixing the as-prepared samples in a 50 mM DMPO (5,5'-dimethyl-1-pyrroline N-oxide) solution with aqueous dispersion for DMPO-OH. The visible light irradiation source was a 300 W Xe arc lamp (PLS-SXE 300, Beijing) system equipped with a UV cutoff filter ($\lambda > 420$ nm). The photoelectrochemical measurements were conducted in a three-electrode system on a CH 660D electrochemical workstation, using the FTO glass with the as-prepared samples as the working electrode, saturated calomel electrode as the reference electrode, and Pt wire as the counter electrode. For the photocurrent test, the working electrode was irradiated from the sample side under a 300 W Xe lamp. Incident visible light was obtained by utilizing a 420 nm cutoff filter. The photocurrent–time dependence at open circuit potential was measured in 0.5 M Na₂SO₄ under chopped illumination.

2.3. Evaluation of Photocatalytic Activity. The photocatalytic activity of the as-synthesized samples was evaluated by removing NO at the ppb level in a continuous flow reactor. The reactor had a capacity of 4.5 L (30 cm × 15 cm × 10 cm), made of polymeric glass and covered with Saint-Glass. A commercial tungsten halogen lamp (100 W) was vertically placed 20 cm above the reactor. A UV cutoff filter (420 nm) was applied to remove UV light for tests of visible light photocatalytic activity. A diagrammatical representation and a photo of the experimental setup are shown in Figure S1 (Supporting Information). The as-prepared sample (0.20 g) was dispersed in distilled water (50 mL) in a beaker via ultrasonic treatment for 10 min and then coated onto two glass dishes (12.0 cm in diameter). The coated dishes were pretreated at 70 °C to remove water in the suspension and were placed at the center of the reactor after being cooled to room temperature. The NO

gas was acquired from a compressed gas cylinder at a concentration of 100 ppm of NO (N_2 balance). The initial concentration of NO was diluted to about 600 ppb via air streaming. The flow rates of the air stream and NO were controlled at 2.4 L min^{-1} and 15 mL min^{-1} , respectively. The two gas streams were then premixed in a three-way valve. The relative humidity was controlled at 50% in the air stream. When the adsorption–desorption equilibrium was achieved, the lamp was turned on. The concentration of NO was measured every 1 min by using an NO_x analyzer (Thermo Scientific, 42i-TL), which also monitored the concentrations of NO_2 and NO_x (NO_x represents $\text{NO} + \text{NO}_2$). The removal ratio (η) of NO was calculated using $\eta (\%) = (1 - C/C_0) \times 100\%$, where C is the outlet concentration of NO after reaction for time t and C_0 represents the inlet concentration after achieving adsorption–desorption equilibrium.

3. RESULTS AND DISCUSSION

3.1. Phase Structure. Figure 1 shows the XRD patterns of the as-prepared samples. The diffraction peaks of BOC are

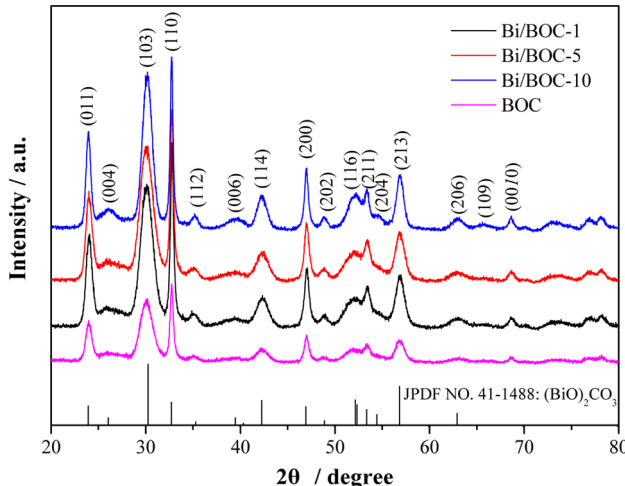


Figure 1. XRD patterns of BOC, Bi/BOC-1, Bi/BOC-5, and Bi/BOC-10 samples.

perfectly indexed as a tetragonal $(\text{BiO})_2\text{CO}_3$ phase (JCPDS-ICDD Card No. 41-1488). After the addition of thiourea to the precursors, all results for the Bi/BOC samples can also be indexed to the $(\text{BiO})_2\text{CO}_3$ phase. The intensity of diffraction peaks increased with the addition of thiourea, which suggests that the addition of thiourea results in improved crystallinity of the samples. The average particle sizes of BOC, Bi/BOC-1, Bi/BOC-5, and Bi/BOC-10 estimated by XRD-Rietveld are 5.4, 5.8, 6.0, and 7.6 nm, respectively. The particle size of the samples increases slightly when the amount of thiourea is less than 5%. When the amount of thiourea is increased to 10%, the particle size is increased up to 7.6 nm. However, no characteristic peaks of Bi can be observed in the XRD patterns, probably because of its low content and high dispersion. Similar circumstances have been reported in other metal/semiconductor photocatalysts. For example, Zan et al. found that it was difficult to prove the existence of metallic Ag in $\text{Ag}/\text{AgX}/\text{BiOX}$ by XRD patterns.⁴¹ Instead, the presence of metallic Ag in the composites was further proved by XPS and HRTEM observations.⁴¹ Zhu et al. found that no diffraction peaks were observed for Au particles due to its high dispersion on the

surface of TiO_2 nanosheets in Au/TiO_2 composites.⁴² The diffraction peaks of Ag were hardly found in the $\text{Ag}/\text{g-C}_3\text{N}_4$ heterostructures due to its low content and high dispersion.⁴³ The changes in diffraction peaks and lattice parameters of $(\text{BiO})_2\text{CO}_3$ in the Bi/BOC samples are also not detectable, which implies that Bi did not enter the lattice of $(\text{BiO})_2\text{CO}_3$ but was only on the surface.⁴⁴ On the basis of the crystal structure of $(\text{BiO})_2\text{CO}_3$, the $(\text{BiO}_2)^{2+}$ and CO_3^{2-} layers are orthogonally intergrown. This internal layered structure would mediate a lower growth rate along a particular axis to form a nanosheet morphology.^{38,45}

3.2. Morphological Structure. The morphologies of the samples were characterized via SEM, TEM, and HRTEM. Typical SEM images at different magnifications are shown in Figure 2. The pure $(\text{BiO})_2\text{CO}_3$ (Figure 2a,b) sample consists of

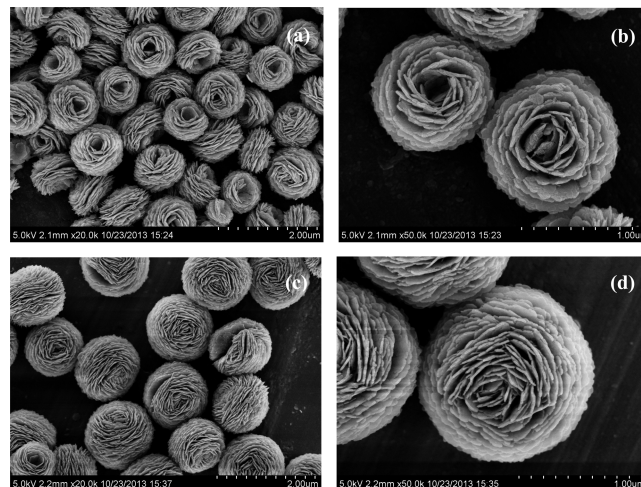


Figure 2. SEM images of BOC (a, b) and Bi/BOC-1 (c, d).

many flowerlike hierarchical microspheres ($\sim 1.0 \mu\text{m}$) self-assembled by nanosheets. The Bi/BOC-1 microspheres (Figure 2c,d) with an increased diameter of about $1.5 \mu\text{m}$ are self-assembled by nanosheets and are more compact.

Figure 3a,b indicates that these microspheres become less regular when the amount of thiourea is increased from 1% to 5%, and this result was caused by the generation of Bi particles. Although the reduced Bi cannot be directly detected in the SEM images because of its small size, the change in sample color (see the inset photos in UV-vis DRS spectra in Figure 6) from white to gray confirms the presence of Bi in Bi/BOC-5. The morphological structure of the sample was further examined via TEM and HRTEM. On the basis of TEM observations (Figure 3c), the Bi/BOC-5 sample consisted of hierarchical microspheres that have solid centers. Figure 3d shows a typical HRTEM image of Bi/BOC-5, which is taken on the edge of a single nanosheet. The lattice spacings are 0.27 and 0.33 nm, which correspond to the (110) crystal plane of $(\text{BiO})_2\text{CO}_3$ and (012) lattice plane of Bi, respectively. This result confirms the presence of Bi particles with an average diameter of 10 nm on the surface of $(\text{BiO})_2\text{CO}_3$ microspheres. The Bi particles were produced by the reduction of thiourea via the reaction given in eq 1. The resulting sulfur is removed by filtering and washing during the preparation.

Figure S2 (Supporting Information) shows the EDX of one point in a microsphere (Figure 3e), and the result indicates that the Bi/O atomic ratio in Bi/BOC-5 is 2.075/S, which is higher

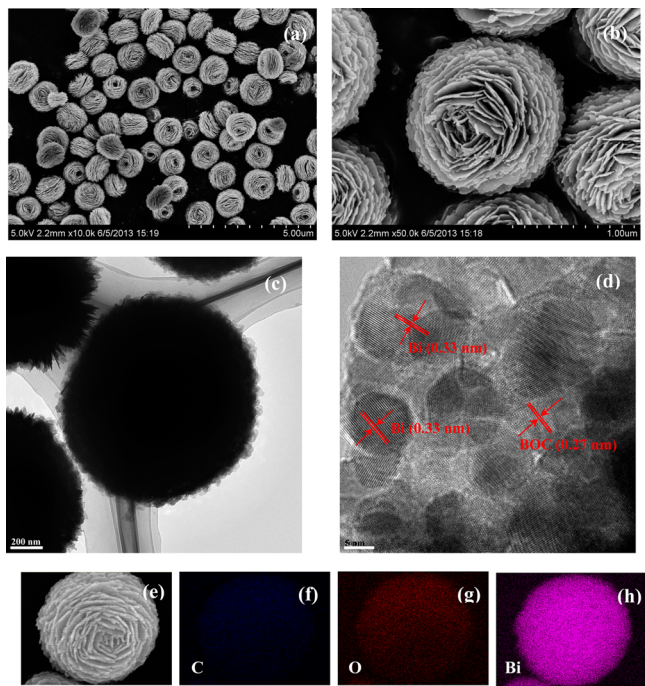
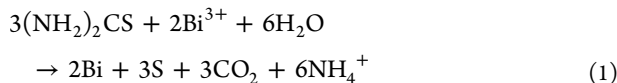


Figure 3. SEM (a, b), TEM (c), and HRTEM (d) images and EDX mapping of a microsphere ((f)–(h) in (e)) of Bi/BOC-5.



than that of BOC (2/5 in $(\text{BiO})_2\text{CO}_3$). This fact implies that elemental Bi particles are actually deposited on BOC, consistent with HRTEM. The EDX mapping of a microsphere in Bi/BOC-5 as shown in Figure 3f–h suggests that the C, O, and Bi elements are distributed uniformly in Bi/BOC-5.

Figure 4a,b obviously shows that the flowerlike hierarchical microspheres partially collapsed and transformed into stacked nanosheets because of the generation of more Bi particles.

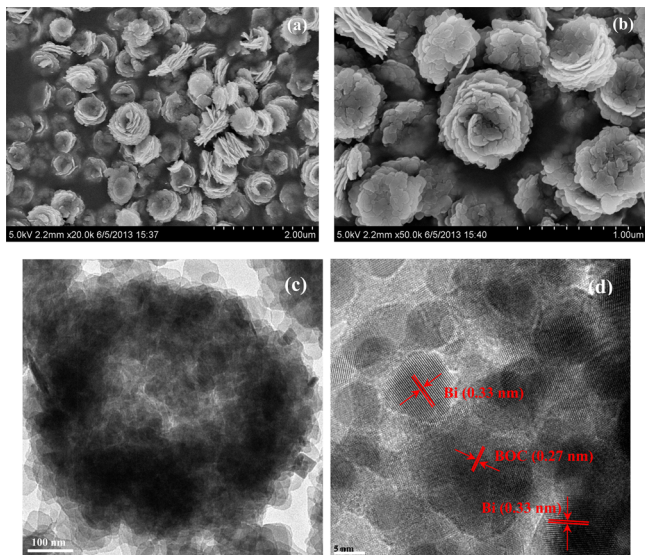


Figure 4. SEM (a, b) TEM (c), and HRTEM (d) images of Bi/BOC-10.

When the amount of thiourea is increased to 10%, more Bi^{3+} ions are reduced to Bi particles, which is confirmed by the change in sample color from gray to dark gray (see the inset of photos in UV-vis DRS spectra in Figure 6). The TEM in Figure 4c indicates that Bi/BOC-10 is hollow in the center and is self-assembled by numerous thin nanosheets. The HRTEM image (Figure 4d) of a single nanosheet shows that some Bi particles with an average diameter of 10 nm are attached on the surface. Except for the lattice spacing (0.27 nm) of the (110) crystal plane in $(\text{BiO})_2\text{CO}_3$, the lattice spacing (0.33 nm) corresponding to the (012) lattice plane of Bi could also be observed.

The BET surface areas of BOC, Bi/BOC-1, Bi/BOC-5, and Bi/BOC-10 are determined to be 46, 45, 44, and $34 \text{ m}^2/\text{g}$, respectively. The obvious decrease in the surface area of Bi/BOC-10 is associated with the morphological change and increased particle sizes (Figure 4). The partial destruction of the hierarchical microspheres resulted in decreased surface areas.

3.3. Chemical Composition by XPS. The surface chemical composition of the Bi/BOC-5 sample was investigated via XPS (Figure 5). Figure 5a shows the survey of the samples, indicating that all of the samples consist of Bi, O, and C. The high-resolution XPS spectra for Bi 4f are shown in Figure 5b. The two strong peaks at 159.1 and 164.4 eV are assigned to $\text{Bi } 4f_{7/2}$ and $\text{Bi } 4f_{5/2}$, respectively, which are the features of Bi^{3+} in $(\text{BiO})_2\text{CO}_3$.⁴⁶ For Bi/BOC-1, Bi/BOC-3, and Bi/BOC-5, samples, two low peaks located at 156.7 and 162.0 eV can be observed, which can be attributed to black metallic Bi, consistent with EDX and HRTEM results (Figure 3d,e).⁴⁷ The peak intensity of metallic Bi is increased with an increasing amount of thiourea. The concentrations of Bi on the surface of Bi/BOC-1, Bi/BOC-5, and Bi/BOC-10 samples are determined to be 0.77, 0.92 and 1.04%, respectively. These findings provide a decent explanation for the color change from white to dark gray, which is also in agreement with the TEM observations. The O 1s peak (Figure 5c) centered at 530.5 eV can be ascribed to the Bi–O bonds in $(\text{BiO})_2\text{CO}_3$. Figure 5d shows the C 1s spectra. The peak at 284.8 eV is caused by the adventitious carbon species, whereas the peak at 288.7 eV is the characteristic peak of CO_3^{2-} in $(\text{BiO})_2\text{CO}_3$. N and S are not detected for the Bi/BOC samples, as shown in Figure S3a,b (Supporting Information), indicating that N and S are not doped in $(\text{BiO})_2\text{CO}_3$ during the synthesis.

3.4. Light Absorption, Charge Separation, and Carrier Lifetime. UV-vis DRS was performed to determine the optical properties of the as-prepared samples. As shown in Figure 6, Bi/BOC-1 exhibits the strongest absorption in the UV region, which can be attributed to its regular morphology. The UV absorption intensity gradually decreased with increasing amounts of thiourea. For Bi/BOC-10, the absorption intensity even becomes lower than that of BOC, which can be attributed to its collapsed microspheres (Figure 4). In the visible light region, the absorption is gradually enhanced with increasing amounts of thiourea. Such absorption is in accordance with the color change of the samples (inset of Figure 6) caused by the appearance of metallic Bi. Notably, a stronger absorption centered at 550 nm is observed, which could be due to the SPR property of metallic Bi. A previous report demonstrated that, as a non-noble metal, Bi displays SPR properties in the near-ultraviolet and visible light range.⁴⁸ This SPR peak is red-shifted in comparison with that for pure metallic Bi (50–100 nm), which can be ascribed to the different sizes of Bi particles.⁴⁸

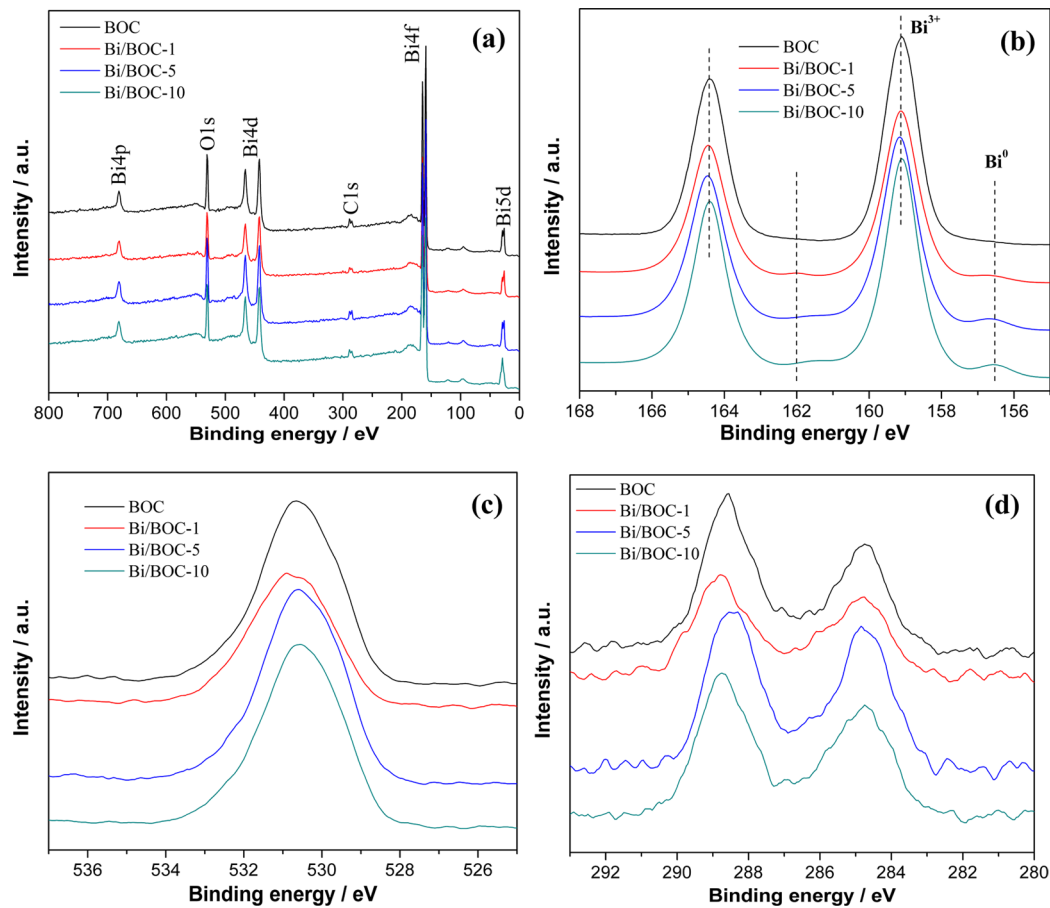


Figure 5. XPS spectra of the samples: (a) survey; (b) Bi 4f; (c) O 1s; (d) C 1s.

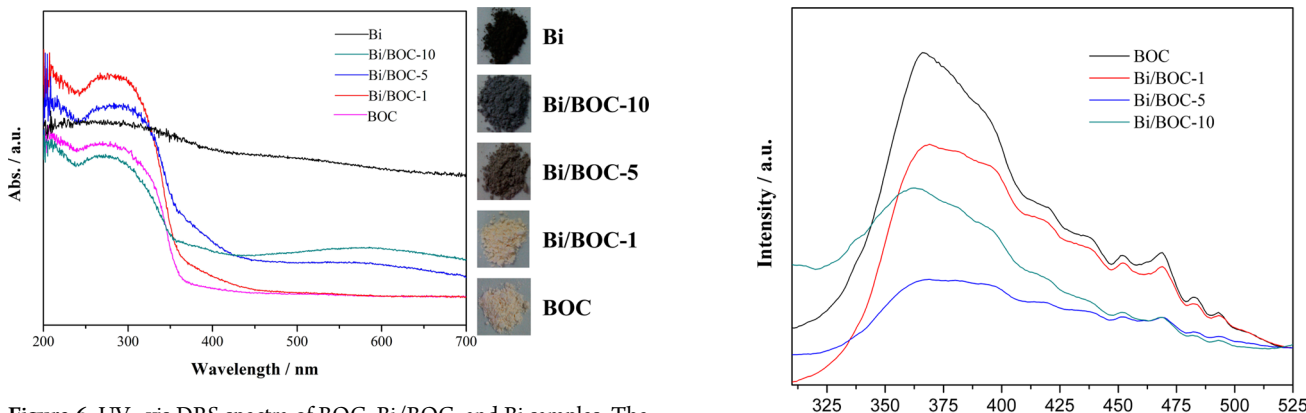


Figure 6. UV–vis DRS spectra of BOC, Bi/BOC, and Bi samples. The insets give photos of sample color.

Wang et al. observed the SPR absorptions of Bi (10–70 nm in size) at around 550 nm, which was attributed to the surface plasmon resonance and light scattering.²⁰ Broad visible absorption bands (450–600 nm) of Bi-based composite samples were also reported by other groups.^{27,28} In general, the formation of metallic Bi on the surface of $(\text{BiO})_2\text{CO}_3$ microspheres can significantly enhance the visible light absorption through the SPR effect.

Photoluminescence (PL) emission is a useful technique in investigating the generation, transfer, and recombination of charge carriers. Figure 7 shows the room-temperature PL spectra of the as-prepared samples. All samples exhibit a broad emission peak centered around 350–400 nm. Generally, a low

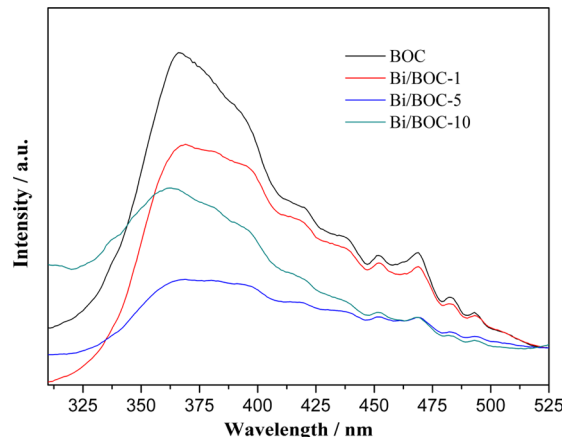


Figure 7. Room-temperature PL spectra of BOC and Bi/BOC.

PL intensity is generally indicative of a high separation efficiency of electron–hole pairs.^{28,49–51} Obviously, the Bi/BOC samples show significantly diminished PL intensity in comparison with pure BOC, which suggests that the deposition of Bi results in a remarkable decline in the recombination rate of electron–hole pairs. This result is supported by the fact that metallic Bi on the surface can function as electron traps and therefore contribute to electron–hole separation.²⁷ Furthermore, the Bi/BOC-5 sample displays the lowest intensity, which suggests that it possess the highest separation efficiency of charge carriers. However, a further increase in the amount of Bi leads to an increase in recombination rate, which implies that

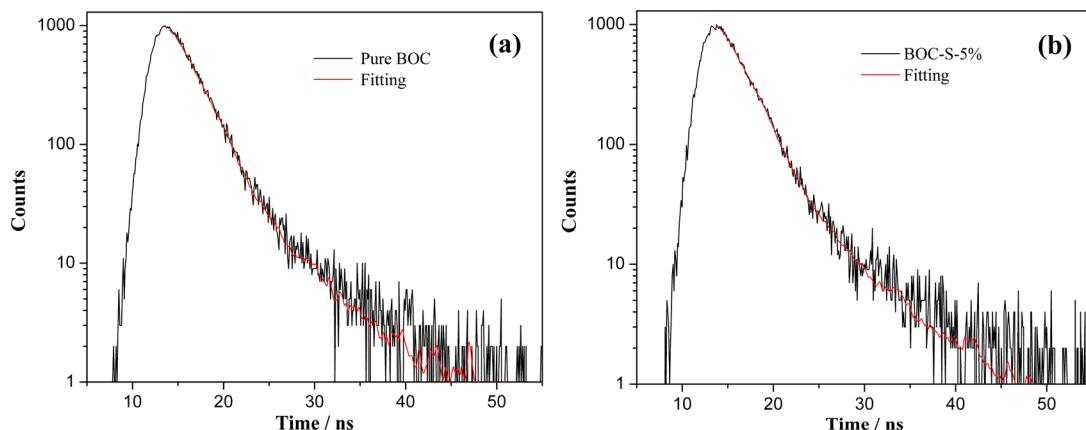


Figure 8. Nanosecond-level time-resolved fluorescence spectra monitored at 440 nm under 375 nm excitation at room temperature for BOC (a) and Bi/BOC-5 (b) samples.

the amount of metallic Bi influences the separation of the charge carriers.

The photophysical properties of photoexcited charge carriers of BOC and Bi/BOC-5 were further analyzed using nanosecond-level time-resolved fluorescence decay spectra, as illustrated in Figure 8. The decay spectra were fitted to obtain the radiative lifetime of the samples. The fitting results are given in Table 1 with two lifetime components (τ_1 , τ_2) and the

radiative lifetimes of all charge carriers are increased by the formation of Bi/BOC heterostructures. The prolonged lifetime of charge carriers can be attributed to the interface transfer of photoexcited electrons between $(\text{BiO})_2\text{CO}_3$ and Bi particles. The prolonged lifetime of charge carriers can increase their probability of participating in photocatalytic reactions before recombination.⁴⁹

Figure S4 (Supporting Information) shows the curves of photocurrent generation for BOC and Bi/BOC-5 electrodes under visible light irradiation. It can be seen that the photocurrent of Bi/BOC-5 is significantly higher than that of BOC, which confirms that the charge separation efficiency of Bi/BOC-5 is greatly enhanced by metallic Bi, consistent with results from room-temperature PL and time-resolved fluorescence decay spectra.⁴⁹

3.5. Photocatalytic Activity, Mechanism, and Photochemical Stability. The photocatalytic activities of the obtained Bi/BOC nanocomposites were evaluated in terms of NO removal in the gas phase. Previous reports have shown that NO is very stable and cannot be photolyzed under light irradiation without photocatalysts.⁴⁶ In the presence of photocatalytic materials, NO can react with photogenerated reactive radicals to produce HNO_3 as the final product.^{39,46} Figure 9a shows the variation of NO concentration ($C/C_0 \%$) with irradiation time for Bi/BOC samples under visible light irradiation with pure $(\text{BiO})_2\text{CO}_3$ and Bi as references.

Table 1. Kinetics of Emission Decay Parameters of BOC and Bi/BOC-5 Samples

| sample | component | lifetime (ns) | rel amt (%) | χ^2 |
|----------|-----------|---------------|-------------|----------|
| BOC | τ_1 | 0.4 | 95.6 | 1.021 |
| | τ_2 | 5.5 | 4.4 | |
| Bi/BOC-5 | τ_1 | 0.7 | 96.0 | 1.010 |
| | τ_2 | 6.9 | 4.0 | |

corresponding relative percentages of charge carriers. The shorter lifetime (τ_1) of BOC is 0.4 ns. After deposition of metallic Bi, the shorter lifetime of Bi/BOC-5 increased up to 0.7 ns. The relative percentage of charge carriers with shorter lifetime of the two samples shows only a slight change. The longer lifetime (τ_2) of charge carriers increased from 5.5 ns for BOC to 6.9 ns for Bi/BOC-5. In addition, the relative percentage of charge carriers with longer lifetime changes slightly for the two samples. These results suggest that the

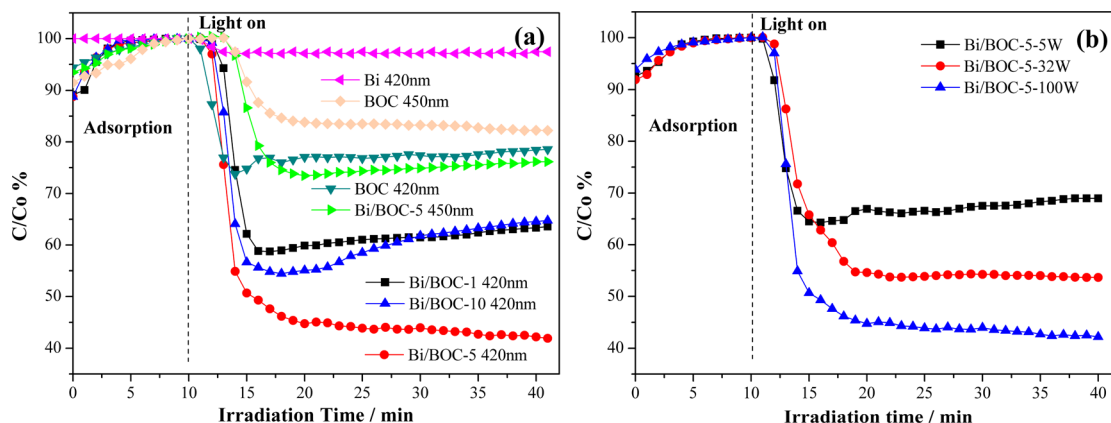


Figure 9. Adsorption process and visible light photocatalytic activity of Bi/BOC, Bi, and BOC samples for the removal of NO at different wavelengths (a) and with different light sources ($\lambda > 420$ nm) (b).

Obviously, metallic Bi exhibits negligible visible light activity for NO removal. This can be attributed to the fact that the potential of electrons generated under visible light irradiation are not negative enough to induce the production of $\bullet\text{O}_2^-$ and the holes are not positive enough for the production of $\bullet\text{OH}$.²² An NO removal ratio of 22% is achieved for pure $(\text{BiO})_2\text{CO}_3$ under visible light irradiation because of surface scattering and the reflecting effect.⁴⁹ The NO removal ratios for Bi/BOC-1, Bi/BOC-5, and Bi/BOC-10 are 36%, 58%, and 34%, respectively, which are more efficient than that of pure $(\text{BiO})_2\text{CO}_3$. Considering the similar morphologies, surface areas, and particle sizes of Bi/BOC-1 and Bi/BOC-5 samples, we can conclude that the metallic Bi can act as an excellent cocatalyst for enhancing visible light photocatalytic activity. Obviously, the Bi/BOC-5 exhibits the most efficient photocatalytic performance, which is significantly higher than that of other types of visible light photocatalysts, such as C-doped TiO_2 (25%), N-doped TiO_2 (36%), C_3N_4 (33%), and BiOBr (21%), and significantly higher than that of Ag-deposited $(\text{BiO})_2\text{CO}_3$ (54%).⁴⁹ These reference photocatalysts were tested under the same conditions. Thus, the discovery that metallic Bi could behave as a superior non-noble-metal-based cocatalyst is of great significance.

However, a further increase in the amount of thiourea to 10% leads to a decrease in photocatalytic activity, which can be ascribed to the collapsed $(\text{BiO})_2\text{CO}_3$ microspheres (Figure 4), decreased BET surface area, increased particle size, and shadowing effect of excess Bi on $(\text{BiO})_2\text{CO}_3$. The collapsed microspheres hinder the rapid diffusion of reaction intermediates and products. The decreased BET surface area reduces the surface active sites in the photocatalytic reaction. The excess metal would become the recombination centers of electron–hole pairs and finally result in decreased activity.^{52,53} The above results indicate that an appropriate amount of metallic Bi could dramatically enhance the visible light photocatalytic activity of $(\text{BiO})_2\text{CO}_3$ microspheres. As is known, NO_2 is an intermediate during the photocatalytic oxidation of NO. For practical application, the generation of NO_2 should be inhibited. Figure S5 (Supporting Information) shows the evolution of NO_2 in the outlet of the reactor system. The fraction of NO_2 produced by Bi/BOC-5 is much lower than that of BOC, which implies that Bi/BOC-5 has a much higher oxidation ability than other samples. This could be explained by the fact that Bi/BOC-5 produces more hydroxyl radicals, which will be discussed later.

When a 450 nm cutoff filter was used, the photocatalytic activities of BOC and Bi/BOC-5 both decreased, but the activity of Bi/BOC-5 remained higher than that of BOC. The photocatalytic activity of Bi/BOC-5 was further tested under different light sources. As shown in Figure 9b, the NO removal ratio under a 32 W energy-saving lamp decreased to 46%. When the lamp was changed to 5 W, the NO removal ratio still reached as high as 31% and was even higher than that of BOC (22%) under 100 W. This result implies that the Bi/BOC-5 sample is a powerful photocatalyst that could work under low-energy lamps, which is definitely favorable for saving energy.

The factors that drive the Bi cocatalyst deposited $(\text{BiO})_2\text{CO}_3$ microspheres to possess such an exceptionally high visible light activity and oxidation ability were further investigated. On the basis of the various characterizations, the highly enhanced photocatalytic activity of Bi/BOC can be ascribed to the synergistic effects of particular factors. First, the SPR effect of metallic Bi propels the Bi/BOC samples to absorb more visible

light, as demonstrated in UV–vis DRS (Figure 6). Meanwhile, the SPR effect photoexcites Bi nanoparticles, thereby enhancing the surface electron excitation and interfacial electron transfer.^{22,49,54,55} Second, given that the Fermi level of metal Bi (-0.17 eV) is higher than the conduction band of $(\text{BiO})_2\text{CO}_3$ (0.20 eV), the photoexcited electrons would transfer from Bi particles to $(\text{BiO})_2\text{CO}_3$ (Figure 10). Once the electrons are

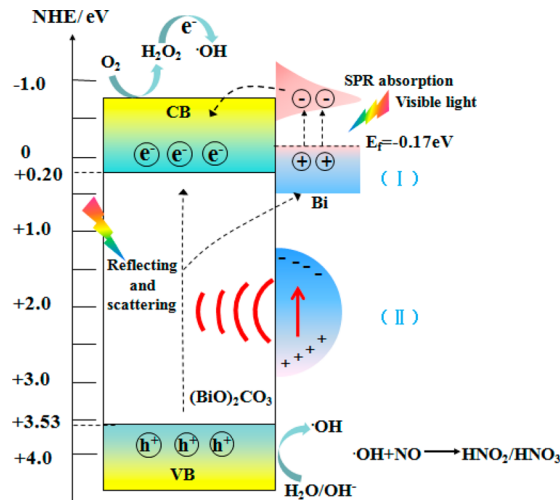


Figure 10. Photocatalytic mechanism scheme of Bi/BOC under visible light irradiation: interface transfer of electrons from $(\text{BiO})_2\text{CO}_3$ to Bi(I) and local electromagnetic field of Bi(II).

released, Bi would shift to more positive potentials to generate positive charges. By accepting electrons from the valence band of $(\text{BiO})_2\text{CO}_3$, Bi would return to its primal state, similar to that of Ag as a cocatalyst in photocatalysis.⁵⁶ Such interface transfer (I) of electrons from $(\text{BiO})_2\text{CO}_3$ to Bi nanoparticles reduces the recombination of electron–hole pairs and increases the lifetime of charge carriers in $(\text{BiO})_2\text{CO}_3$ (Figures 7 and 8 and Figure S2 (Supporting Information)). In addition, the SPR-mediated local electromagnetic field of Bi(II) also radiatively contributes to the generation and separation of electron–hole pairs in $(\text{BiO})_2\text{CO}_3$.⁵⁷ After the separation of electrons and holes, these two kinds of photogenerated charge carriers would be transformed into active species ($\bullet\text{OH}$) that are responsible for the degradation of pollutants. Given that the redox potential of $\text{O}_2/\bullet\text{O}_2^-$ is -0.33 eV, which is more negative than that of the CB of $(\text{BiO})_2\text{CO}_3$, the CB electrons could not reduce the O_2 . Instead, the photoexcited electrons of $(\text{BiO})_2\text{CO}_3$, together with the electrons transferred from Bi, can reduce O_2 to H_2O_2 , given that the redox potential of $\text{O}_2/\text{H}_2\text{O}_2$ is 0.695 eV. The formed H_2O_2 would be further transformed into $\bullet\text{OH}$ by capturing an electron.⁵⁸ Meanwhile, the potential of the holes at the VB of $(\text{BiO})_2\text{CO}_3$ (3.53 eV) is more positive than the redox potential of $\text{OH}^-/\bullet\text{OH}$ (1.99 eV), and therefore the holes can oxidize OH^- into $\bullet\text{OH}$ radicals. Given that $\bullet\text{OH}$ radicals are major reactive oxidation species, they could oxidize NO to for the final HNO_2 and HNO_3 products.

The $\bullet\text{OH}$ radicals are further detected by DMPO-ESR spin trapping, as shown in Figure 11. Under the irradiation of visible light, $\bullet\text{OH}$ radicals can be detected for BOC and Bi/BOC-5 samples. Further observations in Figure 11 indicate that the signal of $\bullet\text{OH}$ radicals for Bi/BOC-5 is much stronger than that of BOC. This result also suggests that Bi/BOC-5 could produce more radicals, which is responsible for its enhanced photo-

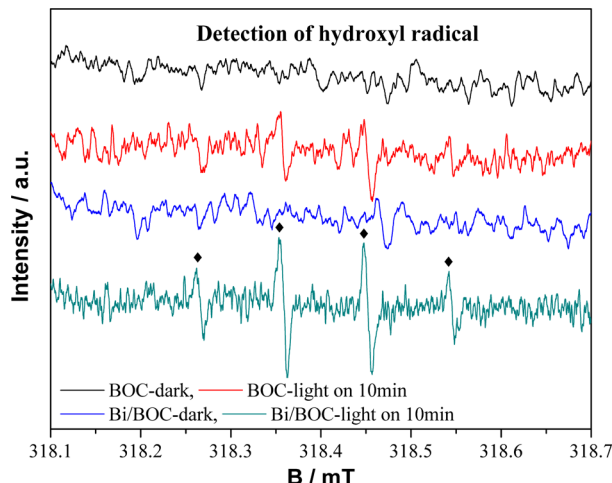


Figure 11. DMPO-ESR spin-trapping spectra of BOC and Bi/BOC-5 for detection of hydroxyl radicals ($\cdot\text{OH}$) in aqueous solution.

catalytic activity and oxidation ability (Figure S5 (Supporting Information)). The generation of more $\cdot\text{OH}$ radicals by Bi/BOC-5 is associated with the SPR effect of Bi particles and transfer of electrons from Bi particles to BOC.²² Figure S6 (Supporting Information) shows that the superoxide radicals ($\cdot\text{O}_2^-$) cannot be detected by DMPO-ESR spin trapping, as the redox potential of $\text{O}_2/\cdot\text{O}_2^-$ is more negative than that of the CB potential of $(\text{BiO})_2\text{CO}_3$. On the basis of the above analysis, the schematic illustration of the photocatalytic mechanism of Bi/BOC under visible light irradiation has been shown in Figure 10. The metallic Bi particles exhibit special noble-metal-like behavior (Ag and Au) in terms of increased visible light absorption and enhanced charge separation and transfer because of the SPR effect, thereby greatly promoting the visible light photocatalytic activity.

An ideal photocatalyst should maintain photochemical stability and durability under repeated irradiation.⁴⁶ Figure 12a shows the repeated visible light photocatalytic activity of Bi/BOC-5. No distinct activity decay is observed after five recycling runs. Figure 12b implies that the Bi/BOC-5 sample could maintain a high activity for 300 min irradiation without obvious deactivation. These results indicate that the Bi nanoparticle deposited $(\text{BiO})_2\text{CO}_3$ microspheres are relatively stable and cannot be easily photocorroded during the photocatalytic process. The stability of Bi/BOC-5 was further confirmed via XRD. As shown in Figure 13a, the XRD patterns

of the sample before and after repeated irradiation are almost the same, which suggests its phase stability. The morphology of Bi/BOC-5 is also well-maintained after repeated irradiation (Figure 13b). Figure S7 (Supporting Information) shows the high resolution XPS spectra of the elements in Bi/BOC-5 after repeated runs. The N-related species cannot be detected (Figure S7), indicating that the oxidation product (NO_3^-) is rare on the catalyst surface and did not accumulate on the surface. Instead, the oxidation product as a HNO_3 vapor would be mainly released in the gas phase and can be easily removed by subsequent absorption (Figure S1a (Supporting Information)). Figure S7 also shows that the XPS spectra for Bi 4f, O 1s, and C 1s for the fresh samples, together with the XRD and SEM of Bi/BOC-5 after repeated runs, which indicates the excellent structural and photochemical stability of Bi/BOC-5. The photochemical stability of Bi/BOC-5 can be attributed to the fact that the reaction intermediates and products could rapidly diffuse in the special hierarchical structures of $(\text{BiO})_2\text{CO}_3$ microspheres, thereby effectively preventing the photocatalyst from deactivation.

4. CONCLUSION

In summary, Bi cocatalyst deposited $(\text{BiO})_2\text{CO}_3$ microspheres with outstanding visible light photocatalytic activity were fabricated via a one-pot hydrothermal method by using thiourea as reductant. During the hydrothermal process, Bi^{3+} was reduced *in situ* to metallic Bi particles by thiourea and then deposited on the surface of $(\text{BiO})_2\text{CO}_3$ microspheres. The introduction of Bi particles has a significant effect on the morphology as well as the optical and electronic properties of $(\text{BiO})_2\text{CO}_3$. The drastically enhanced visible light photocatalytic activity of Bi/BOC samples can be ascribed to the cooperative contribution of SPR effects, efficient separation of electron–hole pairs, and prolonged lifetime of charge carriers by Bi nanoparticles. Among the as-synthesized samples, the Bi/BOC-5 sample with an appropriate amount of Bi particles and well-maintained hierarchical microspheres exhibited the most efficient visible light photocatalytic activity and oxidation ability. The Bi/BOC-5 sample could also work under a low-energy lamp, which is promising for practical applications. The hydroxyl radicals were confirmed to be the main active species for NO photo-oxidation. Bi/BOC could generate more hydroxyl radicals in comparison to BOC, which is responsible for the enhanced oxidation ability. The metallic Bi particles with noble metal-like behavior exerted multiple positive effects on $(\text{BiO})_2\text{CO}_3$, including increased visible light absorption and

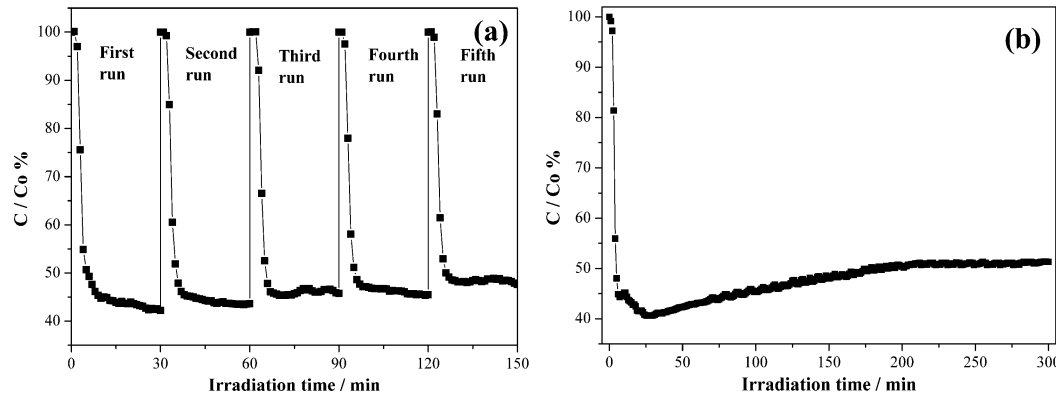


Figure 12. Repeated (a) and long-term (b) photocatalytic activity of Bi/BOC-5 under visible light irradiation for the removal of NO in air.

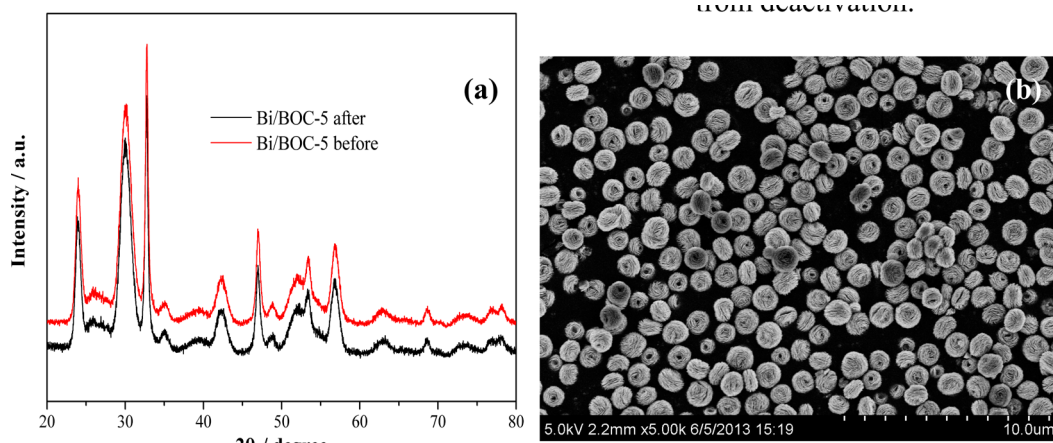


Figure 13. XRD patterns of Bi/BOC-5 before and after repeated irradiation (a) and the SEM images of Bi/BOC-5 after repeated irradiation (b).

enhanced charge separation and transfer because of the SPR effect. This work not only provides new insights into the in situ fabrication of Bi/semiconductor nanocomposites but also opens a new avenue for the modification of photocatalysts with non-noble metals as cocatalyst to achieve a highly enhanced performance.

■ ASSOCIATED CONTENT

● Supporting Information

The following file is available free of charge on the ACS Publications website at DOI: 10.1021/cs501038q.

Diagrammatical representation and a photo of the experimental setup for evaluation of photocatalytic activity, EDX of one point in Figure 3e and EDX mapping of a microsphere in Figure 3e of Bi/BOC-5, XPS spectra of the samples, photocurrent generation of the BOC and Bi/BOC-5 electrodes under visible light irradiation, monitoring of the fraction of NO_2 in the outlet of the reactor system, DMPO-ESR spin-trapping spectra of Bi/BOC-5 for detection of superoxide radicals ($\cdot\text{O}_2^-$) in ethanol solution, and XPS spectra of Bi/BOC-5 after repeated runs ([PDF](#))

■ AUTHOR INFORMATION

Corresponding Authors

*F.D.: e-mail, dfctbu@126.com; tel/fax, +23-62769785-605.

*W.-K.H.: e-mail, keithho@ied.edu.hk.

Notes

The authors declare no competing financial interest.

■ ACKNOWLEDGMENTS

This research was financially supported by the National Natural Science Foundation of China (51108487, 51478070), the Natural Science Foundation of Chongqing (cstc2013jcy-jA20018), and the Innovative Research Team Development Program in University of Chongqing (KJTD201314). This research was financially supported by the research grant of Early Career Scheme (ECS 809813) from Hong Kong, Research fund from The Hong Kong Institute of Education (04022, REG-2, R3429).

■ REFERENCES

- (1) Hoffmann, M. R.; Martin, S. T.; Choi, W.; Bahnemann, D. W. *Chem. Rev.* **1995**, *95*, 69–96.
- (2) Garcia, M. A.; Merino, J. M.; Pinel, E. F.; Quesada, A.; Venta, J.; Gonzalez, M. L. R.; Castro, G. R.; Crespo, P.; Llopis, J.; Gonzalez-Callbet, J. M.; Hernando, A. *Nano Lett.* **2007**, *7*, 1489–1494.
- (3) Yu, J. G.; Yu, X. X. *Environ. Sci. Technol.* **2008**, *42*, 4902–4907.
- (4) Lin, Y. M.; Li, D. Z.; Hu, J. H.; Xiao, G. C.; Wang, J. X.; Li, W. J.; Fu, X. Z. *J. Phys. Chem. C* **2012**, *116*, 5764–5772.
- (5) Choi, H.; Kim, Y. J.; Varma, R. S.; Dionysiou, D. D. *Chem. Mater.* **2006**, *18*, 5377–5384.
- (6) Zhang, L. W.; Man, Y.; Zhu, Y. F. *ACS Catal.* **2011**, *1*, 841–848.
- (7) Zhang, L. W.; Zhu, Y. F. *Catal. Sci. Technol.* **2012**, *2*, 694–706.
- (8) Yang, X. F.; Cui, H. Y.; Li, Y.; Qin, J. L.; Zhang, R. X.; Tang, H. *ACS Catal.* **2013**, *3*, 363–369.
- (9) Yuan, R. S.; Chen, T.; Fei, E. H.; Lin, J. L.; Ding, Z. X.; Long, J. L.; Zhang, Z. Z.; Fu, X. Z.; Liu, P.; Wu, L.; Wang, X. X. *ACS. Catal.* **2011**, *1*, 200–206.
- (10) Chen, X. B.; Shen, S. H.; Guo, L. J.; Mao, S. S. *Chem. Rev.* **2010**, *110*, 6503–6570.
- (11) Chen, X. B.; Mao, S. S. *Chem. Rev.* **2007**, *107*, 2891–2959.
- (12) Zhang, Z. B.; Sun, X. Z.; Dresselhaus, M. S.; Ying, J. Y.; Heremans, J. *Phys. Rev. B* **2000**, *61*, 4850–4861.
- (13) Black, M. R.; Lin, Y. M.; Cronin, S. B.; Rabin, O.; Dresselhaus, M. S. *Phys. Rev. B* **2002**, *65*, 195417–1–195417–9.
- (14) Black, M. R.; Hagelstein, P. L.; Cronin, S. B.; Lin, Y. M.; Dresselhaus, M. S. *Phys. Rev. B* **2003**, *68*, 235417–1–235417–10.
- (15) Volobuev, V. V.; Stetsenko, A. N.; Mateychenko, P. V.; Zubarev, E. N.; Samburskaya, T.; Dziawa, P.; Reszka, A.; Story, T.; Sipatov, A. Y. *J. Cryst. Growth* **2011**, *318*, 1105–1108.
- (16) Tian, M. L.; Wang, J.; Zhang, Q.; Kumar, N.; Mallouk, T. E.; Chan, M. H. W. *Nano Lett.* **2009**, *9*, 3196–3202.
- (17) Wang, F. D.; Tang, R.; Yu, H.; Gibbons, P. C.; Buhro, W. E. *Chem. Mater.* **2008**, *20*, 3656–3662.
- (18) Ma, D. C.; Zhao, J. Z.; Zhao, Y.; Hao, X. L.; Lu, Y. *Chem. Eng. J.* **2012**, *209*, 273–279.
- (19) Qin, F.; Wang, R. M.; Li, G. F.; Tian, F.; Zhao, H. P.; Chen, R. *Catal. Commun.* **2013**, *42*, 14–19.
- (20) Wang, Z.; Jiang, C. L.; Huang, R.; Peng, H.; Tang, X. D. *J. Phys. Chem. C* **2014**, *118*, 1155–1160.
- (21) Zhang, Q.; Zhou, Y.; Wang, F.; Dong, F.; Li, W.; Li, H. M.; Patzke, G. R. *J. Mater. Chem. A* **2014**, *2*, 11065–11072.
- (22) Dong, F.; Xiong, T.; Sun, Y. J.; Zhao, Z. W.; Zhou, Y.; Feng, X.; Wu, Z. B. *Chem. Commun.* **2014**, *50*, 10386–10389.
- (23) Hameed, A.; Montini, T.; Gombac, V.; Fornasiero, P. *J. Am. Chem. Soc.* **2008**, *130*, 9658–9659.
- (24) Jiang, H.; Liu, J.; Cheng, K.; Sun, W.; Lin, J. *J. Phys. Chem. C* **2013**, *117*, 20029–20036.
- (25) He, R. A.; Cao, S. W.; Zhou, P.; Yu, J. G. *Chin. J. Catal.* **2014**, *35*, 989–1007.
- (26) Liu, X. W.; Cao, H. Q.; Yin, J. F. *Nano Res.* **2011**, *4*, 470–482.

- (27) Weng, S. X.; Chen, B. B.; Xie, L. Y.; Zheng, Z. Y.; Liu, P. *J. Mater. Chem. A* **2013**, *1*, 3068–3075.
- (28) Yu, Y.; Cao, C. Y.; Liu, H.; Li, P.; Wei, F. F.; Jiang, Y.; Song, W. *G. J. Mater. Chem. A* **2014**, *2*, 1677–1681.
- (29) Chang, C.; Zhu, L. Y.; Fu, Y.; Chu, X. L. *Chem. Eng. J.* **2013**, *233*, 305–314.
- (30) Chen, R.; So, M. H.; Yang, J.; Deng, F.; Che, C. M.; Sun, H. Z. *Chem. Commun.* **2006**, 2265–2267.
- (31) Cheng, G.; Yang, H. M.; Rong, K. F.; Lu, Z.; Yu, X. L.; Chen, R. *J. Solid. State. Chem.* **2010**, *183*, 1878–1883.
- (32) Zheng, Y.; Duan, F.; Chen, M. Q.; Xie, Y. *J. Mol. Catal. A* **2010**, *317*, 34–40.
- (33) Liu, Y. Y.; Wang, Z. Y.; Huang, B. B.; Yang, K. S.; Zhang, X. Y.; Qin, X. Y.; Dai, Y. *Appl. Surf. Sci.* **2010**, *257*, 172–175.
- (34) Cao, X. F.; Zhang, L.; Chen, X. T.; Xue, Z. L. *CrystEngComm* **2011**, *13*, 1939–1945.
- (35) Madhusudan, P.; Ran, J. R.; Zhang, J.; Yu, J. G.; Liu, G. *Appl. Catal., B* **2011**, *110*, 286–295.
- (36) Madhusudan, P.; Yu, J. G.; Wang, W. G.; Cheng, B.; Liu, G. *Dalton Trans.* **2012**, *41*, 14345–14353.
- (37) Dong, F.; Ho, W. K.; Lee, S. C.; Wu, Z. B.; Fu, M.; Zou, S. C.; Huang, Y. *J. Mater. Chem.* **2011**, *21*, 12428–12436.
- (38) Dong, F.; Lee, S. C.; Wu, Z. B.; Huang, Y.; Fu, M.; Ho, W. K.; Zou, S. C.; Wang, B. *J. Hazard. Mater.* **2011**, *195*, 346–354.
- (39) Dong, F.; Sun, Y. J.; Fu, M.; Ho, W. K.; Lee, S. C.; Wu, Z. B. *Langmuir* **2012**, *28*, 766–773.
- (40) Dong, F.; Liu, H. T.; Ho, W. K.; Fu, M.; Wu, Z. B. *Chem. Eng. J.* **2013**, *214*, 198–207.
- (41) Ye, L.; Liu, J.; Gong, C.; Tian, L.; Peng, T.; Zan, L. *ACS Catal.* **2012**, *2*, 1677–1683.
- (42) Zhu, S.; Liang, S.; Gu, Q.; Xie, L.; Wang, J.; Ding, Z.; Liu, P. *Appl. Catal., B* **2012**, *119*, 146–155.
- (43) Yang, Y.; Guo, Y.; Liu, F.; Yuan, X.; Guo, Y.; Zhang, S.; Guo, W.; Huo, M. *Appl. Catal., B* **2013**, *142*, 828–837.
- (44) Peng, S. J.; Li, L. L.; Tan, H. T.; Wu, Y. Z.; Cai, R.; Yu, H.; Huang, X.; Zhu, P. N.; Ramakrishna, S.; Srinivasan, M.; Yan, Q. Y. *J. Mater. Chem. A* **2013**, *1*, 7630–7638.
- (45) Wu, C. Z.; Xie, Y. *Chem. Commun.* **2009**, 5943–5957.
- (46) Ai, Z. H.; Ho, W. K.; Lee, S. C.; Zhang, L. Z. *Environ. Sci. Technol.* **2009**, *43*, 4143–4150.
- (47) Nyholm, R.; Berndtsson, A.; Martensson, N. *J. Phys. C: Solid St. Phys.* **1980**, *13*, L1091–L1096.
- (48) Toudert, J.; Serna, R.; Castro, M. J. *J. Phys. Chem. C* **2012**, *116*, 20530–20539.
- (49) Dong, F.; Li, Q. Y.; Zhou, Y.; Sun, Y. J.; Zhang, H. D.; Wu, Z. B. *Dalton. Trans.* **2014**, *43*, 9468–9480.
- (50) Huang, Q.; Tian, S.; Zeng, D.; Wang, X.; Song, W.; Li, Y.; Xiao, W.; Xie, C. *ACS Catal.* **2013**, *3*, 1477–1485.
- (51) Li, K.; Chai, B.; Peng, T.; Mao, J.; Zan, L. *ACS Catal.* **2013**, *3*, 170–177.
- (52) Ren, J.; Wang, W. Z.; Sun, S. M.; Zhang, L.; Chang, J. *Appl. Catal., B* **2009**, *92*, 50–55.
- (53) Young, C.; Lim, T. M.; Chiang, K.; Scott, J.; Amal, R. *Appl. Catal., B* **2008**, *78*, 1–10.
- (54) Wang, P.; Huang, B. B.; Dai, Y.; Whangbo, M. H. *Phys. Chem. Chem. Phys.* **2012**, *14*, 9813–9825.
- (55) Wang, D. J.; Xue, G. L.; Zhen, Y. Z.; Fu, F.; Li, D. S. *J. Mater. Chem.* **2012**, *22*, 4751–4758.
- (56) Cheng, H.; Huang, B.; Wang, P.; Wang, Z.; Lou, Z.; Wang, J.; Qin, X.; Zhang, X.; Dai, Y. *Chem. Commun.* **2011**, *47*, 7054–7056.
- (57) Atwater, H. A.; Polman, A. *Nat. Mater.* **2010**, *9*, 205–213.
- (58) Xiang, Q. J.; Yu, J. G.; Cheng, B.; Ong, H. C. *Chem. Asian. J.* **2010**, *5*, 1466–1474.